Automatic segmentation of coronary morphology using transmittance-based lumen intensity-enhanced intravascular optical coherence tomography images and applying a localized level-set-based active contour method

Shiju Joseph
Asif Adnan
David Adlam

SPIE.

Automatic segmentation of coronary morphology using transmittance-based lumen intensity-enhanced intravascular optical coherence tomography images and applying a localized level-set-based active contour method

Shiju Joseph, Asif Adnan, and David Adlam*
University of Leicester, Department of Cardiovascular Sciences, Cardiovascular Research Centre, Glenfield General Hospital, Leicester LE3 9QP, United Kingdom

Abstract. Lumen segmentation from clinical intravascular optical coherence tomography (IV-OCT) images has clinical relevance as it provides a full three-dimensional perspective of diseased coronary artery sections. Inaccurate segmentation may occur when there are artifacts in the image, resulting from issues such as inadequate blood clearance. This study proposes a transmittance-based lumen intensity enhancement method that ensures only lumen regions are highlighted. A level-set-based active contour method that utilizes the local speckle distribution properties of the image is then employed to drive an image-specific active contour toward the true lumen boundaries. By utilizing local speckle properties, the intensity variation issues within the image are resolved. This combined approach has been successfully applied to challenging clinical IV-OCT datasets that contains multiple lumens, residual blood flow, and its shadowing artifact. A method to identify the guide-wire and interpolate the lost lumen segments has been implemented. This approach is fast and can be performed even when guide-wire boundaries are not easily identified. Lumen enhancement also makes it easy to identify vessel side branches. This automated approach is not only able to extract the arterial lumen, but also the smaller microvascular lumens that are associated with the vasa vasorum and with atherosclerotic plaque. © *2016 Society of Photo-Optical Instrumentation Engineers (SPIE)* [DOI: 10.1117/1.JMI.3.4.044001]

1 Introduction

Intravascular optical coherence tomography (IV-OCT) is now widely used for the clinical assessment of atherosclerotic plaque, as this technology provides high-resolution (axially $\approx 15~\mu$m resolution) cross-sectional images of the coronary arterial wall.[1] While structural images can provide a high-contrast view from these cross-sections, clinical image interpretation from two-dimensional (2-D) sections requires considerable experience leading to significant interobserver variability.[1] Automated assessment can reduce this error and produce more consistent image interpretation. Various techniques have been reported for lumen segmentation,[1–8] stent strut detection,[7] and plaque characterization.[1,9] These approaches are either semi or fully automated.

Lumen segmentation and three-dimensional (3-D) reconstruction of the coronary artery has been a key objective due to the clinical applicability of this approach for the assessment and treatment of coronary stenosis. In IV-OCT images, lumen regions are visualized as a signal-sparse region surrounded by the bright tissue regions constituting the vessel wall. Thus, the wall–lumen interface provides a high degree of contrast and this is generally exploited by various techniques to extract the lumen boundary. Some of the methods previously employed include image thresholding,[1] A-line intensity-variation analysis,[2,3]

intensity difference-dependent cost function and its minimization approach,[4,5] and labeling methods using Markov random field (MRF).[7] Alternatively, a combination approach with expectation maximization (EM) for labeling and graph-cut for lumen segmentation has been reported.[8] All these techniques use the tissue region as the reference from which to determine the boundary. The lumen geometry generated can then be refined using an active contour method (ACM).[6,8]

The IV-OCT images in reports describing application of these lumen segmentation methods are usually selected to have optimal image quality. However, the real-world context of clinical IV-OCT frequently generates more challenging images resulting from complex anatomy, artifacts, and disease. For example, although rapid pullback technologies have eliminated the need for proximal balloon occlusion, during clinical image acquisition images are frequently partially distorted by blood artifacts[10] [Fig. 1(a)]. Additionally, diseased arteries may present highly altered lumen shapes [Fig. 1(b)] that can be challenging for current segmentation tools. Morphological operations,[6] prior to the lumen segmentation, can be applied to the IV-OCT images to minimize the effect of blood artifacts. However, complete removal is not guaranteed, especially when blood is flowing very close to, or in continuity with the luminal wall. In such situations, cost function minimization methods[4,5]
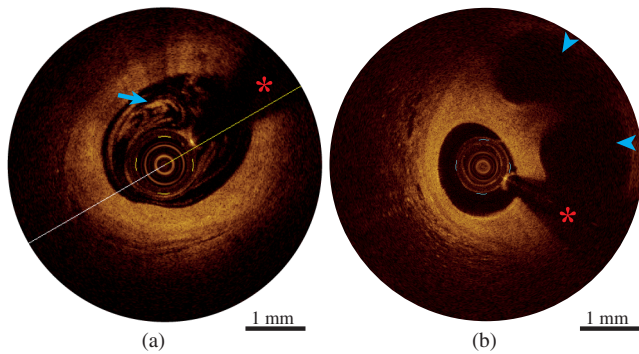

Fig. 1 Examples of lumen segmentation challenges from *in vivo* clinical IV-OCT images. (a) Residual blood circulation (arrow) within the lumen during imaging with associated shadowing artifact on the tissue region. (b) Image cross-section showing multiple lumens (arrow heads) in a diseased coronary section. The marking * indicates the guide-wire and its shadow artifact on the image.

also fail and manual intervention is advised.[1,5] More importantly, when the intensity of a tissue region is reduced by the shadowing effect, intensity-dependent segmentation methods may fail to distinguish the luminal region. In such situations, statistical property-based labeling methods such as MRF[7] and EM+graph-cut[8] may be able to identify tissue regions, but systematic assessment of this strategy on challenging "real world" clinical datasets has not been reported. There is, therefore, a need for an automatic lumen segmentation tool that can account for such variations.

To create a fully automated lumen segmentation method, in this study, a technique to enhance lumen intensity was applied, thereby focusing the segmentation approach on the lumen instead of the tissue region. A statistically formulated level-set-based ACM segmentation method was then employed to extract the lumen. To demonstrate the capability of this combined approach, challenging *in vivo* clinical IV-OCT images with blood-flow artifacts and multiple lumens were successfully analyzed. The proposed method is also capable of compensating for guide-wire artifacts and yields the correct lumen contours for side-branch ostia.

2 Methods

Figure 2 shows the steps developed to automate the lumen segmentation process. Steps 1 to 5 were implemented individually for each frame in the pullback dataset. The lumen region in every frame was enhanced and then a localized region-based level-set segmentation method was applied to segment the lumen. Once the lumen geometry was segmented from every frame, a 3-D vessel shape was rendered. The lumen enhancement method enabled the identification of guide-wire artifacts and side-branch openings, which were then compensated after the lumen contour was obtained (see Fig. 2).

2.1 *Transmissivity-Dependent Intrinsic Lumen Contrast*

An attenuation coefficient-based strategy has been widely used for OCT image enhancement[11] and also as a quantitative diagnostic parameter.[12] It has been employed for coronary artery tissue characterization[13] and classification of plaque constituents.[9,14] Due to blood clearance, luminal regions are largely devoid of any scattering material and, therefore, have very low attenuation coefficients, making this an ineffective contrasting agent. However, the reciprocal of attenuation coefficient gives the transmissivity of the region. Thus, the lower the attenuation, the higher the transmissivity and vice-versa. Subsequently, in a transmissivity map for an IV-OCT image, the luminal regions are expected to have bright contrast while tissue regions remain dark. This enables direct visualization of all lumen regions that can then be segmented with an appropriate technique.

The transmissivity (τ) map (inverse of attenuation coefficient), for a radial A-line was estimated using a depth resolved method,[11,12] given by

$$\tau(z) = \frac{1}{\mu(z)} = \frac{2 \int_z^\infty I(u) \mathrm{d}u}{I(z)}, \tag{1}$$

where, $\mu(z)$ is the attenuation coefficient, $I(z)$ is the OCT signal along the radial A-line of the IV-OCT image, and z is the depth position. In Eq. (1), it was assumed that all the light
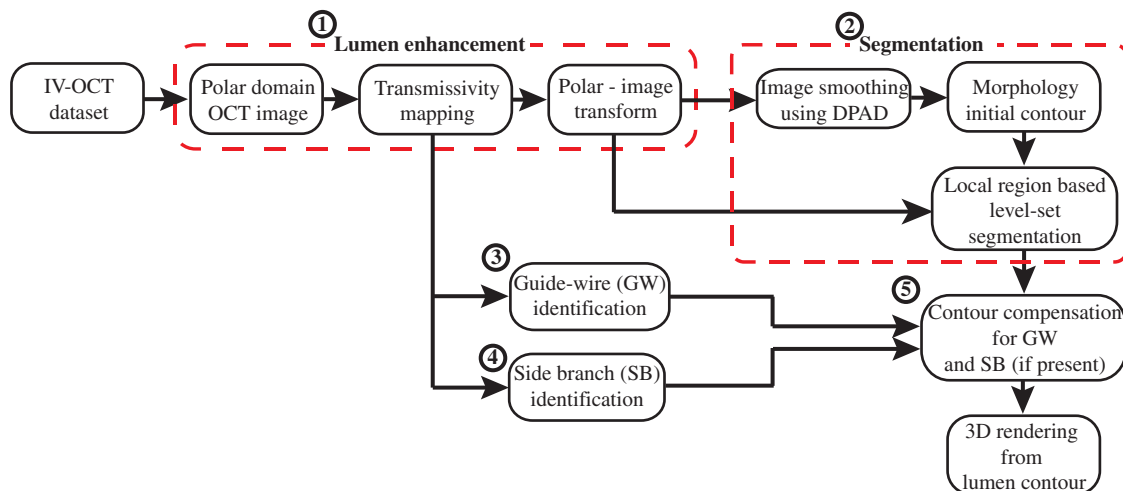

Fig. 2 Block diagram illustrating the steps followed for segmenting the lumen from clinical *in vivo* IV-OCT images. The encircled numerals 1 to 5 indicate the order of the steps. DPAD, detail preserving anisotropic diffusion.

was attenuated within the imaging depth and that a certain fraction of attenuated light was always received at the detector. For practical implementation, the infinity was replaced by total image depth, D. Since the transmissivity property was employed only to enhance the contrast of the luminal regions, intensity exponentiation[11] was performed before a transmissivity calculation was implemented. Thus, Eq. (1) becomes

$$\tau(z) = \frac{2 \int_z^D I^n(u)\mathrm{d}u}{I^n(z)}. \tag{2}$$

From Eq. (2), it could be observed that the transmissivity map of a given IV-OCT image could change as the exponential factor n was varied. Therefore, the effect of exponentiation on τ was analyzed and an appropriate value was determined that provided suitable contrast for the lumen.

The application and optimization of the technique are shown in Fig. 3. Based on Eq. (2), a set of transmittance maps for Fig. 3 were generated using $n = 1, 2, 4, 6, 10$ values. As shown in Fig. 3(c), the log-scale compressed transmittance value for the lumen regions [marked (II)] increased with the n value, whereas, other regions such as tissue regions [marked (III)] and background regions [marked (IV)] had negligible changes when compared to the lumen region. Though the

catheter region [marked (I) in Fig. 3(c)] had transmissivity levels similar to the lumen region for a given n value, it did not affect the lumen segmentation.

From Fig. 3(c), it was evident that increasing the exponential value improved both the τ value and the relative contrast of the lumen region. As the objective was to enhance the lumen contrast, the log-scale transmissivity values at the lumen region were compared with the background region, as it had higher transmissivity when compare to the tissue region. Using Eq. (3), interlayer contrast was determined for every transmissivity map obtained for $n = 1, 2, \ldots, 10$.

$$C = \frac{\log(\tau_{lm}) - \log(\tau_{bg})}{\log(\tau_{lm}) - \log(\tau_{bg})} \times 100, \tag{3}$$

where C was the calculated contrast in percentage, τ_{lm} and τ_{bg} were the transmissivity values, respectively, for a selected region of interest pixels in the lumen (lm) and background (bg) regions. The mean of the $\log(\tau)$ value at (5×1) pixels for each region in the polar-format IV-OCT image were used. The plot in Fig. 3(d) shows the change in the calculated contrast for various n values. The profile shows that the contrast improves nonlinearly for $n \leq 6$ values, beyond which there was only minor improvement. Also, at $n = 6$, about 50% contrast was achieved, which was
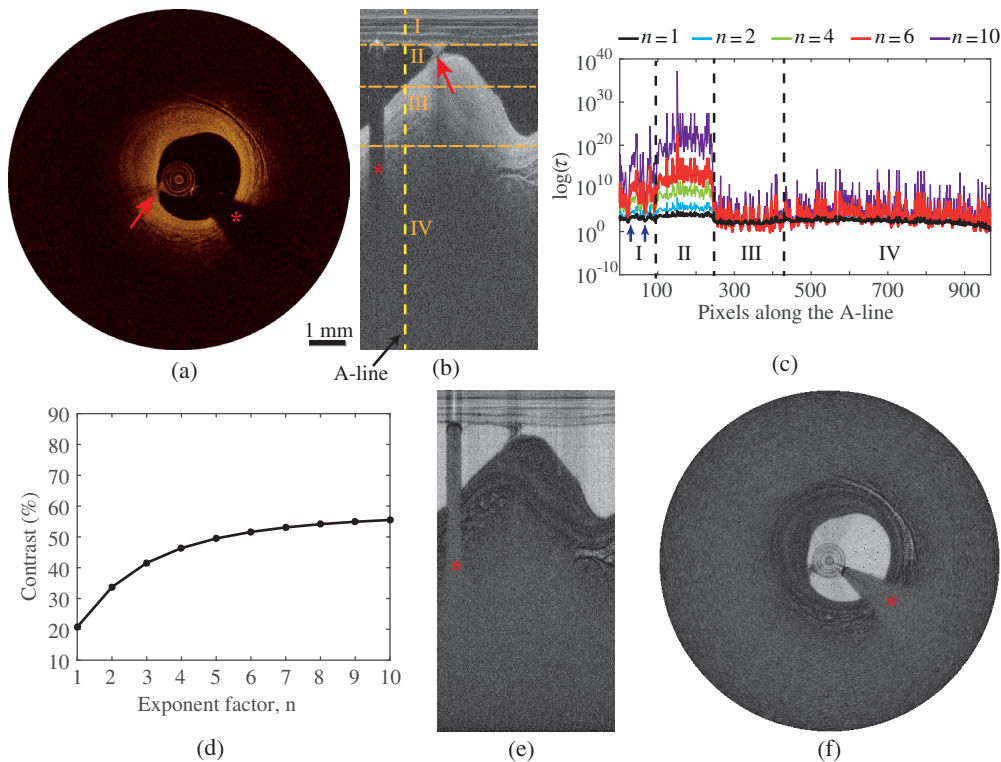

Fig. 3 Transmittance-dependent contrast generation and optimization for the luminal region in an IV-OCT image. (a) *In vivo* clinical IV-OCT image and (b) polar format image of (a). (c) Transmittance profile along the A-line marked in (b), for n different exponent values [in Eq. (2)]. The subregions in (c) corresponds to areas marked in (b) where identifiers denote, I. catheter, II. lumen, III. tissue, and IV. background. From (c) it is evident that, with increasing exponent value, the log-scale transmittance is mainly enhanced in the lumen. (d) Interlayer contrast for n values, calculated using log-scale transmittance at lumen and background regions (marked II and IV, respectively) along the A-line in (b). Contrast between the two layers increased with n value and at $n = 6$, 50% improvement in contrast was achieved. (e) Transmittance-dependent intensity image of (b) obtained using $n = 6$. (f) Display format image of (e). Arrows in (a) and (b) points the blood volume between the wall and the catheter. The marking * indicates the guide-wire.
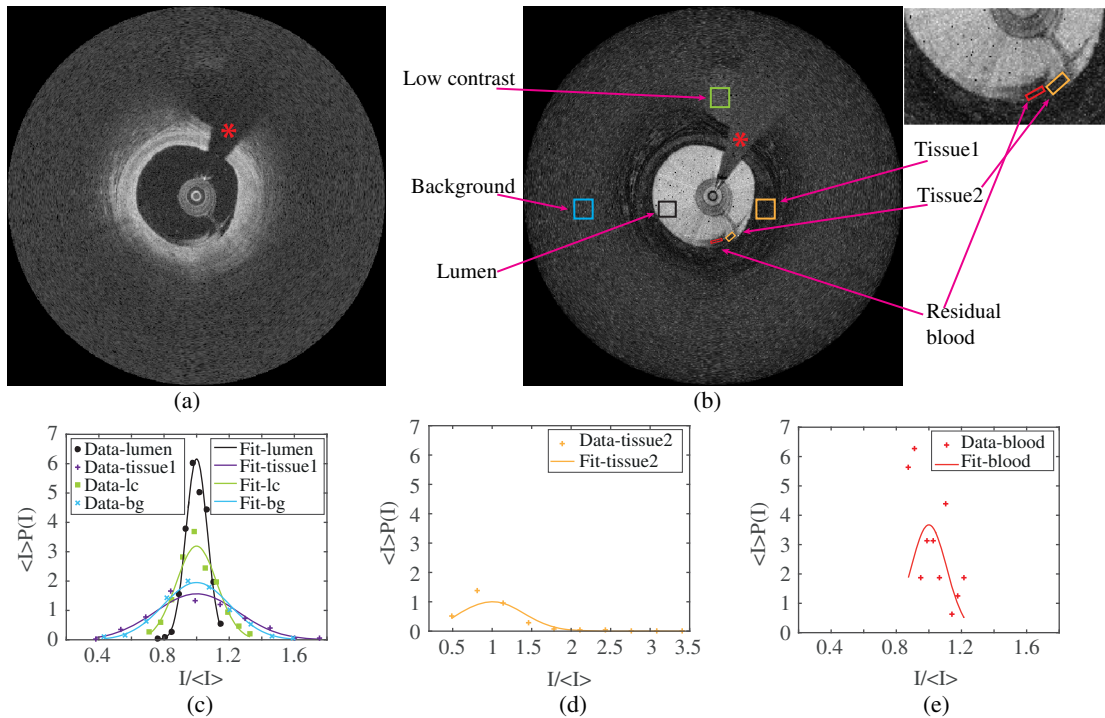
Fig. 4 Speckle analysis of the lumen intensity-enhanced IV-OCT image. (a) Normal clinical *in vivo* IV-OCT image. (b) Intensity-enhanced counterpart of (a). Inset: Enlarged view of the tissue 2 and residual blood regions in (b). (c–e) Distribution of pixel intensities at selected regions, marked in (b). In all the plots, the Gaussian fit was applied to the data. All regions except the blood flow region exhibit a Gaussian distribution. The marking * indicates the guide-wire and its shadow artifact on the image.

found to be adequate enough to generate good lumen contrast as shown in Figs. 3(e) and 3(f). Throughout the study, $n = 6$ was used to calculate the transmissivity coefficients for the IV-OCT images.

The transmissivity mapping method enabled selective enhancement of the lumen intensity and the luminal regions were readily visualized. The catheter area, which had similar transmissivity as the lumen region, appeared as embedded within the latter [as in Fig. 3(f)]. Therefore, a direct segmentation of the lumen was now possible from display format images, without the need for sequential removal of the catheter and its protective sheath.[4]

To obtain lumen intensity-enhanced IV-OCT images, first transmissivity maps were generated with $n = 6$ value, from every polar domain IV-OCT image. Then a log-scale compression was applied to the transmissivity maps to reduce the dynamic range which was both inherently present and resulted from the exponentiation. The resultant was then converted to an 8-bit grayscale intensity image. Thus the obtained lumen intensity-enhanced polar-format images were transformed to image co-ordinates [Fig. 3(f)].

2.1.1 Speckle analysis of lumen intensity-enhanced IV-OCT images

The lumen segmentation method employed in this study utilized the speckle distribution properties of the image. Therefore, a speckle analysis was carried out to determine the type of speckle distribution exhibited by the lumen intensity-enhanced IV-OCT image. Figures 4(a) and 4(b) show a normal IV-OCT image and its lumen intensity-enhanced version, respectively. The image used here was also a representative model of challenges

commonly observed in IV-OCT datasets. A lumen region, with residual blood circulation between the 6 and 5 o'clock positions but otherwise with high-contrast, was clearly identifiable in both Figs. 4(a) and 4(b). A low-contrast lumen of a side-branch was also visible in both images Figs. 4(a) and 4(b). The image in Fig. 4(b) was smoothed with a (2×2) averaging filter and then speckle analysis carried out for selected regions—lumen (black square), tissue [tissue 1 and tissue 2 (orange squares)], low-contrast lumen (green square), background (blue square), and residual blood artifacts (red square) markedly shown in Fig. 4(b). The histogram of pixel intensities at these regions demonstrated that all regions [see, Figs. 4(c) and 4(d)], except for the residual blood flow region [see Fig. 4(e)] had a Gaussian distribution. From Fig. 4(c), it is also evident that the mean and SD values for the main and the low-contrast lumen regions were different when compared to their respective surrounding regions. It should be noted that the speckle in OCT images are generally considered to have a Rayleigh-type distribution.[15] This change in speckle distribution may be attributed to the interpolation method used for constructing such images from the polar-format counterpart.[16]

A statistics-based segmentation method has the potential to discriminate lumen areas; when the residual blood artifact was very close to the lumen boundary and had similar intensities to the vessel wall. This was demonstrated by the regions at the 6 and 5 o'clock positions of Figs. 4(a) and 4(b), where two sets of streaky structures—the outer blood flow and a tissue region jutting into the lumen—are present. The speckle distribution at the residual blood flow region [see Fig. 4(e)] had a different type of distribution when compared to regions shown in Figs. 4(c) and 4(d).

2.2 Localized Region-Based Level-Set Active Contour Method

Application of the contrast enhancement technique, discussed in Sec. 2.1, allowed direct visualization of the lumen and if the blood were effectively cleared, morphological operations would be adequate to extract the lumen shapes. However, in *in vivo* clinical IV-OCT images, complete blood clearance is not always possible. The presence of blood in the lumen would reduce the transmissivity in those regions and, therefore, appears darker in the transmissivity maps. Thus images generated from these maps would also contain image artifacts for the luminal regions. In such cases, intensity-dependent methods would require manual intervention to accurately extract the luminal boundaries. To overcome these issues and to automatically segment the lumen boundaries, a local region-based ACM method[17] with a level-set function was employed in this study. This segmentation approach followed the method proposed by Wang et al.[18] that had been demonstrated for medical images such as ultrasound and MR images, but had not been implemented for IV-OCT datasets. Its essential derivation steps have been summarized in Appendix.

As it is an active contour-based image segmentation method, an energy functional consisting of an image-dependent data term and a length penalizing regularizer function that smooths the curve was first defined. The image-dependent energy functional was defined locally using the speckle distribution property of the image. As discussed in Sec. 2.1.1 and shown in Fig. 4, a Gaussian-type speckle distribution was appropriate, therefore, the level-set approach proposed by Wang[18] et al. was suitable. The image-dependent energy functional term was defined for a local neighborhood using the Gaussian probability distribution function shown in Eq. (5). The image-dependent energy minimization term was derived on the basis that the contour segments the region so as to have a maximum a posteriori probability (MAP),[18] see Eq. (6). Since it is a local-region-based method, this minimized energy term was localized by incorporating a window function into the energy equation, as shown in Eq. (8). The obtained local energy functional was integrated over the entire image region to obtain the energy functional term for the whole image.

The total energy functional employed in this study is shown in Eq. (12). It can be observed that this energy functional was also dependent on a level-set function, ϕ, which embedded the active contour as its zero level-set. Thus, ϕ provided an implicit representation of the evolving curve. The total energy functional

in Eq. (12) was minimized to achieve the segmentation. The image-dependent parameters, i.e., local mean (u_i) and standard deviation (SD) (σ_i) that minimized the energy functional are shown in Eqs. (13) and (14), respectively. Finally, using a gradient descent method, the equation [see, Eq. (15)] describing the curve evolution to minimize the energy was determined.

The implementation of the local-region-based ACM method consisted of the following steps:

Step 1.1 The initial level-set function ϕ_i for the lumen segmentation was derived from the image itself by taking a distance transform of the corresponding intensity thresholded binary image.

Step 1.2 The local mean, u_i, and local SD, σ_i, were calculated using Eqs. (13) and (14), respectively, for a given ϕ_i. In both equations, $\mathcal{W}$ was a kernel window of $(K \times K)$ size applied to the image, I, for localization. The H_ε was determined using Eq. (10) and subsequently used for determining $M_{i,\varepsilon}$.

Step 1.3 The u_i and σ_i values were then used to solve the right-hand side of Eq. (15). In Eq. (15), a suitable weighting constant, ν, value was used.

Step 1.4 Using the gradient descent method, Eq. (15) was solved to obtain a new level-set function, ϕ_{i+1}, i.e., $\phi_{i+1} = \phi_i + (\mathcal{E}\Delta t)$, where $\mathcal{E}$ represents the solution obtained in step 1.3. Δt is the time-step.

Steps 1.1 to 1.4 were computed in a loop with N number of iterations, during which the contour was expected to trace the true lumen boundary. The parameters such as kernel window size—K, weighting constant—ν, time-step—Δt, and N were tuned to achieve accurate lumen segmentation. For implementing this segmentation method for a pullback dataset, these parametric values were generally determined for a selected frame and then applied for every frame in the whole pullback dataset. If the segmentation was not fully achieved for any of the frames, then the parametric values were altered and recomputed for the affected frames. For a pullback dataset, the lumen segmentation was implemented sequentially for every frame in the stack. All the computational calculations involved in steps 1.1 to 1.4 were performed in MATLAB®.

The binary image required for step 1.1 was obtained by the following approach, shown in Fig. 5. The image was first smoothed using an edge-preserving anisotropic diffusion[19] method [see Fig. 5(b)] and then from its histogram the upper value of the full-width at half maximum for the largest peak
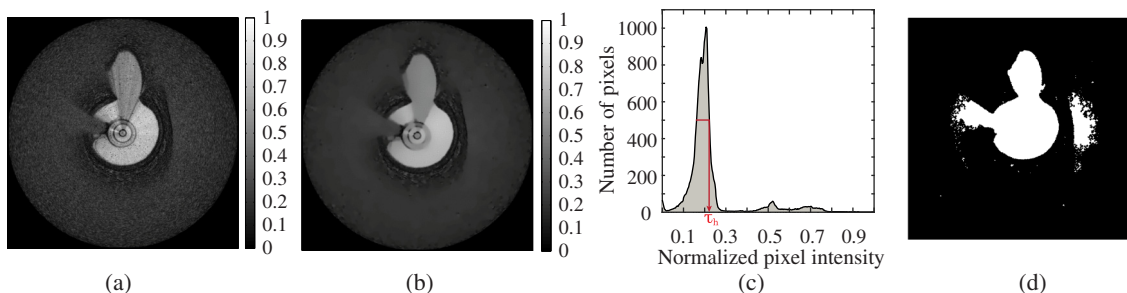

Fig. 5 Initialization of the level-set function using image thresholding. (a) Lumen intensity-enhanced IV-OCT image. (b) Image smoothing using anisotropic diffusion scheme to reduce the speckle noise and to enhance the low SNR regions. (c) Histogram plot of pixel intensities of image in (b). The value at τ_h was used as the threshold value. (d) Binary image of (b) obtained using the threshold value determined from the histogram.

— $N = 50$
— $N = 250$
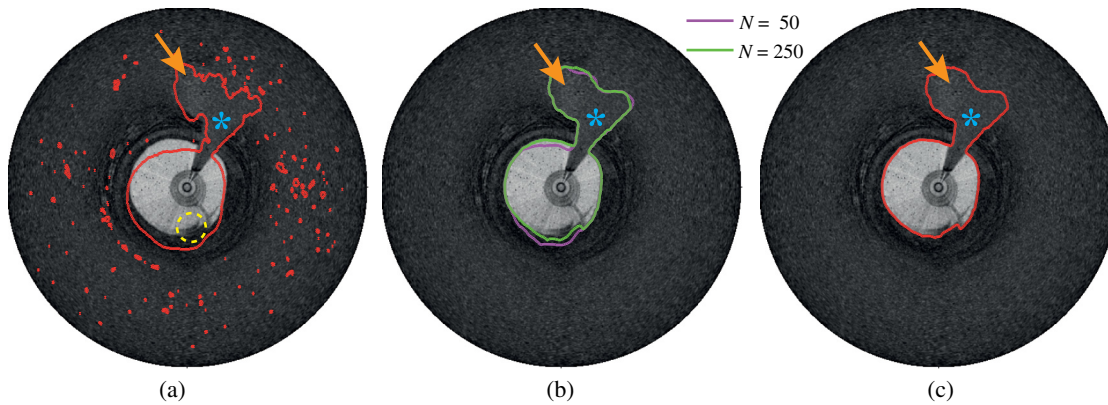
(a)　　　　　　　　(b)　　　　　　　　(c)

Fig. 6 Local-region-based level-set-based lumen segmentation method employing statistical properties of the image. (a) Initial contour at zero level-set of ϕ obtained from a binary image. (b) Intermediate zero level-set contours after N iterations. (c) Final zero level-set contour after 500 iterations (Video 1). The encircled region in (a) highlights the lumen region which due to residual blood artifact appear as part of tissue region (darker area), however the final contour in (c) was able to segment the lumen correctly. The marking * indicates the guide-wire and the arrow points to the low-contrast region. The parametric values $K = 41$, $N = 500$, $\nu = 0.05 \times 255 \times 255$, and $\Delta t = 0.01$ were used. The enlarged view of encircled region in (a) can be seen in the inset of Fig. 4(b) (Video 1, MPEG, 74 KB) [URL: http://dx.doi.org/10.1117/1.JMI.3.4.044001.1].

[see Fig. 5(c)] was determined. This value [τ_h in Fig. 5(c)] was used as the threshold value to generate the binary image [as in Fig. 5(d)]. This process was performed automatically for every frame in the pullback. Additionally, morphological operations using bwareaopen, imfill, and imclose functions of MATLAB® were performed on the binary images to remove small isolated regions and to close holes if any were present. These imperfections were found to increase the computation time for segmentation.

The ϕ_i of step 1.1 was obtained by applying a MATLAB® function, bwdist—Euclidean distance transform function, to the binary mask [as in Fig. 5(d)]. The active contour was the zero level-set of the ϕ. Initial ϕ derived in this manner ensured that the initial contour was in close proximity to the lumen boundary, therefore, the lumen boundary can be obtained very quickly. Because the initial contour was close to the lumen boundary, ϕ did not undergo a large shape change as it evolved. Therefore, no regularizer function, used by Wang et al.[18] to control the deviation in level-set function from its initial shape, was incorporated into the total energy functional in Eq. (12). The length penalizing regularizer function ($\mathcal{L}$) included in Eq. (12) controlled the smoothness of the contour.

Figure 6 demonstrates the lumen segmentation process using a lumen intensity-enhanced IV-OCT image. The binary mask required for initializing ϕ was generated using the histogram approach shown in Fig. 5. The ϕ_i obtained from a different binary mask was used to demonstrate the active contour evolution and segmentation of the lumen in the presence of artifacts. Figure 6(a) shows the zero level-set of the ϕ_i overlaid on the top of the image to be segmented. Small noisy contours that appear along with the larger contours, in Fig. 6(a), were artifacts in the binary mask. In actual implementation, these small artifacts would be removed from the binary image through the morphological operations. As contour evolution progresses, these noisy contours observed in Fig. 6(a) disappear in Fig. 6(b). $N = 500$ iterations were required to obtain the true lumen boundary. The final lumen contour in Fig. 6(c) closely follows the lumen boundary. The lumen contour at the low-contrast region [marked by

the arrow in Fig. 6(c)] also fit its boundaries accurately. Though the lumen contour contained the guide-wire artifact [see Fig. 6(c)], this could be compensated by the method proposed in Sec. 2.3.

Although in Fig. 6, $N = 500$ iterations were employed, generally ≤50 iterations were required. This is because the ϕ_i was usually determined from the same image so the initial contour was close to the actual lumen contour.

2.3 Guide-Wire Correction Using Dynamic Programming Method

The guide-wire identification and its artifact correction is a requirement for the segmentation of most *in vivo* clinical IV-OCT images. In the Maximum Intensity Projection (MIP) of a polar-format, log-compressed IV-OCT image pullback stack the guide-wire appears as a continuous feature[2,5] [see Fig. 7(a)]. The guide-wire segmentation is usually achieved from the MIP images by means of intensity thresholding[2] or boundary detection through a dynamic programming method.[5] As shown by the overlaid contour in Fig. 7(a), some regions (marked by bold arrows) were missed out in the intensity thresholding method. This would result in underestimation of the guide-wire width as shown in Fig. 7(b). While the DP method may succeed in segmenting such guide-wire portions, it may fail to distinguish a guide-wire region from a side-branch if both were overlapping [see the double arrow area in Fig. 7(a)]. If the boundaries were indistinct, accurate segmentation may not be possible and would require manual interference.

In this study, the bright reflecting centerline [see Fig. 7(c)] of the guide-wire was segmented using a DP approach.[20] As a strongly reflective[1] body, it generally appears the brightest (metallic stents can also appear bright). From Fig. 7(c), the optimal path, $P_{C_1 \to C_N}$ for the guide-wire starts from the first column C_1 and traces up to the last column C_N. From all possible paths, the optimal path had the highest cumulative cost, with the cumulative cost, $G_{k,j}$, for a partial path $P_{C_i \to C_j}$ defined as in Eq. (4).
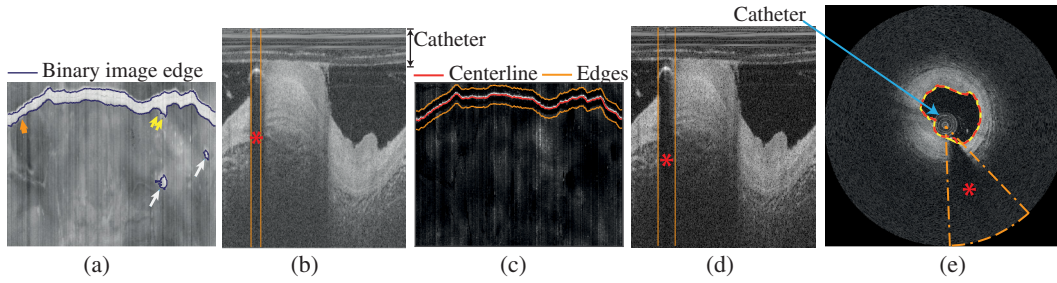
Fig. 7 Illustration of the guide-wire segmentation approach. (a) Guide-wire segmentation by intensity thresholding of the maximum intensity projection (MIP) map of the pullback stack. The slim arrow points to the side-branches. Bold arrow, guide-wire region underestimated, double arrow, side-branch misidentified as part of guide-wire. (b) Effect of underestimation of the guide-wire thickness. (c) Centerline contour obtained using dynamic programming method. Edge contours are the boundaries of the guide-wire obtained by shifting the centerline contour upward and downward by half the maximum width (i.e., 25 pixels) of the guide-wire. (d) Effect of underestimation of the guide-wire thickness. (e) The segment of the lumen contour (a red dash dash line) within the identified guide-wire area (an orange dash dot dash line) was masked out and then interpolated over the region to obtain the final lumen contour (a continuous cyan yellow line). The asterisks in (b), (d), and (e) denote the guide-wire. The images in (b) and (d) have their background regions cropped out for this figure and enlarged for better view.

$$G_{k,1} = I_{k,1}$$

$$G_{k,j} = I_{k,j} + \max_{k-n \leq k \leq k+n} \{G_{k,i}\} \quad \text{where,} \quad 1 < j \leq N \quad \text{and} \quad i < j.$$

$$(4)$$

The "I" in Eq. (4) represents the projection map [see Fig. 7(c)] from which the optimal path was determined. In Eq. (4), the subscripts (k, j) refer to the rows and columns of the cumulative cost matrix, G, respectively. Since the optimal path had the highest cumulative cost, the path retrieval process starts from the location for the highest cumulative value, i.e., $\max\{G_N\}$ is the maximum value in the last column of the G matrix. The process then retraces back through the preceding columns up to the first column, finding for every column the location (or row) of the connected optimum predecessor, within the archived steps.

The index "$k \pm n$" in Eq. (4) is the window length within which the path search was constrained. In this study, $n = 10$, i.e., a window length of $(2n + 1) = 21$ was used for detecting the guide-wire. The red curve in Fig. 7(c) traces the path detected by the DP-based guide-wire detection method.

The width, d, of the guide-wire within a frame was assumed to be $d = d_{max}$, where d_{max} was the largest width observed in the pullback. Then two contours at distances of $(d/2)$ from the detected guide-wire centerline were traced out on either side, as shown in Fig. 7(c). As each column of the map represents an IV-OCT image from a pullback dataset, the radial co-ordinates for the two edges of the guide-wire artifact can be determined from the locations of the two outer contours at a given column. Once the guide-wire edge co-ordinates were determined, the lumen contour portions within it were masked out and the ends interpolated [as shown in Fig. 7(e)].

Here, it was assumed that every frame had the same width for the guide-wire artifact. However, in practice, narrowing and broadening of the guide-wire shadow are commonly observed in clinical datasets. Since the maximum width was considered, in some frames the guide-wire artifact width would be overestimated [see Fig. 7(d)]. However, this had a negligible effect on the final lumen contour as the lumen segment at the guide-wire shadow region and its vicinity were interpolated using the curve shape information of a much larger length.

2.4 Compensation of Lumen Contour at Low-Intensity Segments of Side Branch

It was observed that sometimes the sections of the segmented lumen contour (from Sec. 2.2) were inconsistent with the expected lumen shape. Such irregularities were especially observed for the side branch lumen segments that were either extending beyond the imaging range or had diffused boundaries. The presence of blood artifacts further deteriorates the contrast of these regions. Also, sometimes parts of a side-branch would appear to fold over into the image due to limitations in the ranging depth.[10] In such scenarios, lumen segmentation methods cannot guarantee an accurate lumen contour for the affected regions. Corrupted lumen contours can affect the lumen quantification methods such as geometrical analysis[3,4] of the contour to identify bifurcation points of the side branches. To overcome this, a scheme is presented wherein low-intensity lumen regions of the side branches were identified and subsequently the erroneous contour sections were masked out.

The implementation of the compensation method consisted of the following steps:

Step 2.1 An intensity map was first constructed using the mean intensity for the last "N" rows of the polar-format lumen intensity-enhanced IV-OCT images in the pullback.

Step 2.2 By intensity thresholding, the side-branch location within a frame and the frame number were automatically identified from the intensity map.

Step 2.3 Using the location information from step 2.2, the side-branch and its surrounding regions were selected from the frame and then a sobel-type image gradient was applied.

Step 2.4 By intensity thresholding, low gradient regions were suppressed and a binary image containing only strong lumen boundaries was constructed.

Step 2.5 The empty A-lines of the binary image that had strong lumen gradient regions on either side were automatically identified as regions requiring contour compensation.

The implementation of the method is shown in Fig. 8. As shown in Fig. 8(b), the locations of the side-branches within
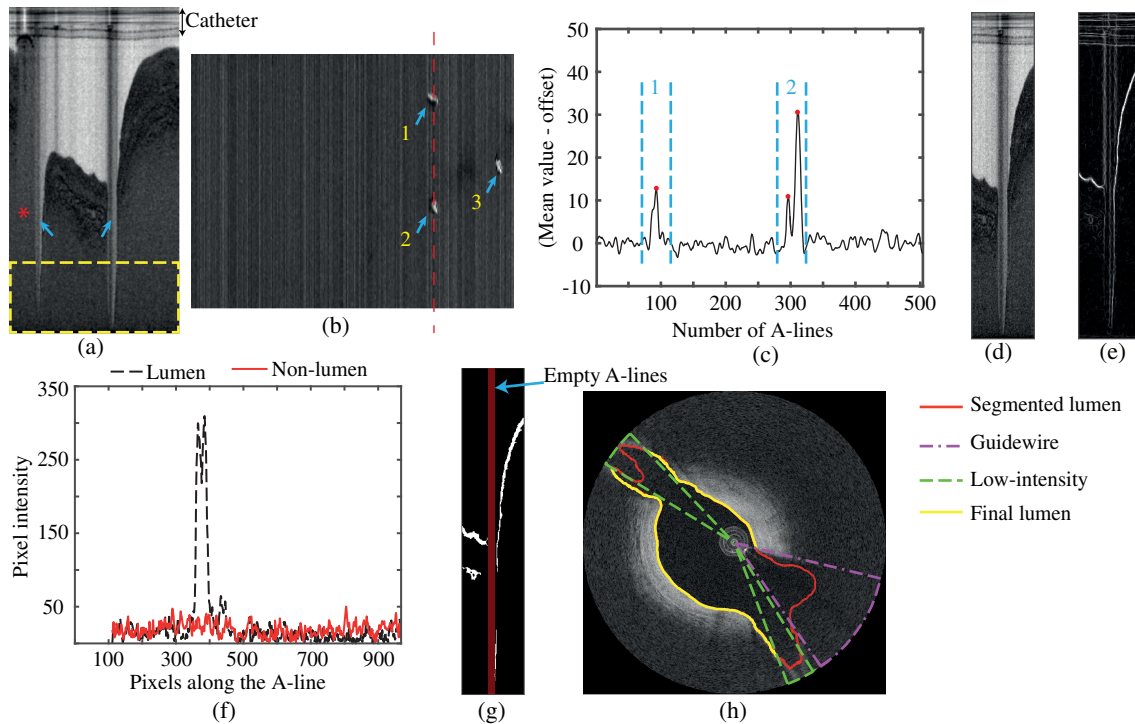
Fig. 8 Compensation of the lumen contour discrepancy at low-intensity lumen boundaries of the side-branches. (a) Lumen intensity-enhanced IV-OCT image with side-branch regions (pointed arrows). (b) Mean intensity map for the last $N = 100$ rows [yellow dotted box in (a)] of every image in the pullback stack. The side-branches (numbered) are conspicuous. (c) Line profile of the values along the dotted line in (b) for the image in (a). (d) Using the side-branch location information in (b) second side-branch in (a) was segregated. (e) Image gradient operation applied to (d) for identifying low intensity lumen regions of the side branch. Only true lumen boundaries had a strong gradient. (f) Comparison of true lumen and noisy regions in the gradient image. (g) Intensity thresholded binary image of (e). The catheter region has been masked out. Only the lumen regions that had a strong gradient are observed in the binary image. The empty A-lines (shaded red) between these regions were identified as low-contrast regions, as highlighted by the overlay plot in (g). (h) The low-intensity lumen regions of the side-branches in (a) were thus identified and the lumen contour within these regions was masked out to obtain the final lumen. The asterisk in (a) denotes the guide-wire.

a pullback can be easily visualized through step 2.1. High contrast was achieved for side-branch regions, as shown in Fig. 8(c). This was possible because the lumen intensity enhancement (see Sec. 2.1) enabled lumen regions of the side-branches to have higher intensities than the surrounding regions, especially when the side branches extended beyond the ranging depth [as in Fig. 8(a)]. The intensity thresholding in step 2.2 was applied and a binary image containing only the side branches was constructed. From this binary image, the frames containing the side-branches can be easily identified.

The determination of the extent of the side-branch, within a frame, was achieved by identifying the corresponding peak [as in Fig. 8(c)] and then averaging the values of the 20 sample points on either side of the peak. The A-lines within the selected peak region which had this average value was considered as the span of that particular side branch. It can be noticed that this was a rough estimate, as it depended upon the "N" value used to generate the mean intensity map [e.g., Fig. 8(b)] and also on the accurate determination of the peak positions. However, the rough estimate of the side-branch location was adequate for determining the low-contrast lumen regions of the side branch. From Fig. 8(c), the widths of the side-branches in Fig. 8(a) were determined in terms of A-lines.

The implementation of step 2.3 for Fig. 8(a) is shown in Figs. 8(d) and 8(e). The image gradient operation enhanced the lumen regions with strong boundaries while the low-contrast regions appeared noisy [see Fig. 8(e)] and is further shown in Fig. 8(f). Before, step 2.4 was applied the strong gradient locations of the catheter were masked out. Accurate knowledge of the catheter boundaries was not necessary as the lumen region of the selected side-branch was always away from the catheter. In the case of Fig. 8(e), all the rows ≤100 were masked out.

The binary image obtained for Fig. 8(e), from step 2.4, contained only lumen regions with strong boundaries [see Fig. 8(g)]. This was achieved by applying a unique threshold value for every A-line in the gradient image. The threshold value, "th," for a given A-line was defined as the sum of the mean (M) and twice the SD (i.e., th = $M + 2 \times$ SD) of the gradient profile. Any gradient value below the threshold was assumed to be noise and was suppressed. Subsequently, a binary image containing only the strong lumen boundaries was generated. Sometimes, localized blood artifacts would appear in the binary image, but due to their relatively smaller size they were removed by morphological operations such as bwareaopen and imclose MATLAB® functions. Using step 2.5, the span of the low-contrast lumen regions were determined from the binary image.

Table 1 Computational time required for each of the image processing methods on an HP EliteBook laptop.

Method	Image size	Computing time (s)
Transmissivity mapping	968×504	1.15
Polar-Image transform	968×504	2.89
Edge preserved smoothing	512×512	4.3
Lumen segmentation (20 iteration)	512×512	<4
Guide-wire	504×270	0.47
Low-contrast side-branch	$968 \times 504 \times 270$	47.54

The lumen contour (from Sec. 2.2) was then corrected by masking out the contour sections over the low-contrast regions. The contour correction of the IV-OCT in Fig. 8 is shown in Fig. 8(h) where both the initial uncorrected and the final contour has been displayed. The low-contrast segments obtained by this method has been overlaid alongside the detected guide-wire segment (from Sec. 2.3).

2.5 *Computational Implementation*

The image processing methods, lumen enhancement, followed by its segmentation, and contour correction for artifacts, were implemented in MATLAB® 2015a, 64-bit version-8.5 (MathWorks, Natick, Massachusetts). The programs were first applied on an HP EliteBook 8770w laptop (Intel Core i7-3720QM, 32GB RAM, and 64 bit Windows 7). The computational time required for each method is listed in Table 1. On a per frame basis, the largest computing time was required for the anisotropic diffusion-based edge preserved smoothing, whereas the guide-wire segmentation from the projection image of a pullback dataset required only 0.47 s to compute.

Computational analysis for the validation studies (discussed in Sec. 4) was however performed at the high-performance computing (HPC) facility of the University of Leicester, UK. The computing jobs were submitted as serial jobs and allocated only one node and one processor core with an 8 GB memory. The HPC system accepted all the job submission for the validation study and serially computed every dataset at the same time. This greatly reduced the total computational time.

3 Materials

A St Jude C7-XR IV-OCT (St Jude inc., "ILUMIEN™") clinical system was used for all imaging. This system has a fixed A-scan rate of 50 kHz and frame-rate of 100 Hz. All the imaging was performed with a pullback speed of 20 mm/s and travel length of 54 mm. Each circumferential scan consists of 504 A-lines, which were then transformed into polar form as cross-sectional images. A clinical grade catheter (C7 Dragonfly, St Jude inc., "ILUMIEN™") was used throughout the study. The lumen intensity enhancement and the segmentation were further applied to an anonymized clinical IV-OCT dataset. Imaging was performed after contrast flushing for blood clearance. Human imaging was undertaken on clinical grounds as part of procedures undertaken with informed consent according to institutional guidelines for the University Hospitals of Leicester, UK.

4 Validation Experiments

The image processing approach presented in Sec. 2 was applied to 30 randomly selected clinical IV-OCT pullback datasets and then compared with manual segmentation, performed by two independent image analysis experts. The first observer, O1, manually analyzed every 20th frame in each of the 30 datasets, while the second observer, O2, performed the same for first 15 datasets. Each pullback dataset consisted of 270 frames. The selected datasets contained images corrupted by blood artifacts and catheter rotation issues. Four pullback datasets had the last 20 to 40 frames completely lost to blood circulation. Six dataset contained metallic stents while three dataset had bioreabsorbable vascular scaffolds; the remainder of the datasets did not have any stent or scaffolds. All 30 datasets contained the guide-wire artifacts.

Both O1 and O2 observers manually segmented the lumen region using the roipoly MATLAB® function. The lumen contour was then generated as an outline for the segmented region. For manual segmentation, normal IV-OCT images [such as Fig. 7(h)] were used, while the computed approach used the lumen intensity-enhanced IV-OCT images, as in Fig. 6. The degree of agreement between any two segmentations, i.e., O1 versus O2, O1 versus At, and O2 versus At (where At refers to the automatic method), was carried out using an intraclass coefficient (ICC) method.[4] For any two segmentations, the ICC method compared the radial distance (measured in pixels) of the lumen contour points from the image center. The radial distance error (i.e., differences in the measured radial distance) between any two approaches was also performed. The interpolated lumen segment for the guide-wire artifact was not considered for the comparison.

For manual analysis of the guide-wire, polar-format images [e.g., Fig. 7(b)] were used and both observers visually determined the radial distance (measured in pixels) of the bright center location from the top of the image. The identified guide-wire distances (by O1 and O2 observers) and also those extracted automatically (Sec. 2.3) were compared using the ICC and Bland–Altman (BA) methods.

To validate the automatic method presented in Sec. 2.4, both manual observers O1 and O2 only analyzed the side-branches with low-contrast lumen, out of the 81 side branches that were present in the 30 datasets. O1 observer analyzed 28 side branches while its subset of 18 side-branches were evaluated by observer O2. Polar-format log-scale compressed normal IV-OCT images were used and the angular width and location of the signal-sparse lumen regions of the side-branches were determined in terms of the A-line separations.

5 Results

The ICC comparison of the automated lumen segmentation with both manual segmentations exhibited a high correlation, as O1 versus At and O2 versus At had 0.912 and 0.893 correlation values, respectively. The difference in the radial distances between the computed and manually segmented lumens showed an average error of -1.82 ± 18.6 and -1.43 ± 18.8. As expected, both manual segmentations closely matched each other and the radial distance error was about -0.5 ± 1.3.

Automatic versus manual segmentation analysis of the guide-wire centerline also showed a high correlation, as shown in Fig. 9. In Fig. 9(a), manual observations are plotted against the automatic measurement and a strong linear relationship was observed. The BA plot, in Fig. 9(b), compares each observer
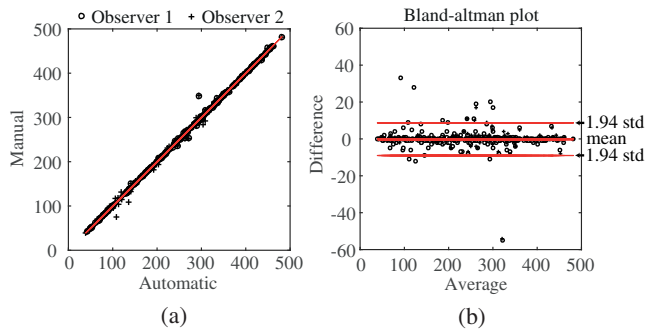
Fig. 9 Validating the guide-wire segmentation. (a) Comparison of manual and automatic guide-wire segmentation results. The A-line position of the guide-wire center determined by respective methods was compared. A strong linear correlation can be observed. (b) BA plot compares the differences between each observer versus the automatic method.

Table 2 Comparison of the manual (O1 and O2) and automatic (At) methods for segmentation of lumen and guide-wire and identification of low-contrast regions in side branches.

		O1 versus At	O2 versus At	O1 versus O2
Lumen	ICC	0.912	0.893	0.999
	Diff	−1.815 ±18.6037	−1.4258 ± 18.793	−0.521 ± 1.339
Guide-wire	ICC	0.999	0.999	1.0
	BA	−0.1569 ± 8.9951	−0.0725 ± 8.9792	−0.3478 ± 2.215
Side branch	TP (%)	60	59	75
	FP (%)	13	13.5	8.75
	Dice	0.78 ± 0.2	0.78 ± 0.2	0.87 ± 0.14

(O1 and O2) to the automatic method and shows a narrow spread for both cases. A mean bias of $\sim -0.16 \pm 9$ and $\sim -0.07 \pm 9$ was obtained with respect to observers O1 and O2, respectively.

The contour correction approach (in Sec. 2.4) was validated with manual observations (by O1 and O2 observers), which detected the signal sparse lumen boundaries at the side-branches, where the lumen segmentation approach would possibly fail. Between the two observers, O1 and O2, 75% (true positive rate, TP value) of the 18 side-branches which had the degraded lumen segments were detected correctly with 8.75% false positives (FP). Comparison of the observer against the automatic approach shows that 60% of the 28 (O1 observer) and 18 (O2 observer) side-branches with such lumen segments can be correctly identified with about 13.5% FP. The average Dice's coefficient for the angular spread of the detected signal sparse side-branch lumen region versus the two observers' measurement was about 0.78 ± 0.2. Comparatively lower TP values were observed here because the low signal-to-noise ratio (SNR) pixel intensities at these regions resulted in variations of the boundary locations determined by each method. Since this approach is employed only to mask out the corrupted lumen contour segments, such TP values were adequate.

A summary of the results for validation of lumen and guide-wire segmentations and automatic identification of low contrast lumen regions of the side branches has been presented in Table 2.

6 Additional Capabilities

The intensities of all luminal regions can be enhanced by the transmittance mapping method (Sec. 2.1). With the proposed level-set-based lumen segmentation method, multiple lumens can be simultaneously segmented, as shown in Fig. 10(a). The steps illustrated in Fig. 2 and described in Sec. 2.2 were followed for this segmentation. It can be noticed that all the larger lumens and smaller microvascular lumens [at 11 and 12 "o" clock positions in Fig. 10(a)] were segmented by this approach. Common lumen segmentation methods[1,2,4] have generally been shown for single simple lumen geometries. While observation of multiple lumens [as in Fig. 10(a)] may not be common, lumen dissections are not uncommonly observed in coronary artery diseases.[10,21] It can also be shown that the proposed method can also extract elements of the plaque associated with microvasculature, a prevalent feature related to atherosclerotic plaque progression.[22,23] By applying the proposed segmentation approach to a pullback, it was possible to not only construct a 3-D vessel geometry, but also visualize the microvascular branch associated with the main artery [see Fig. 10(b)].
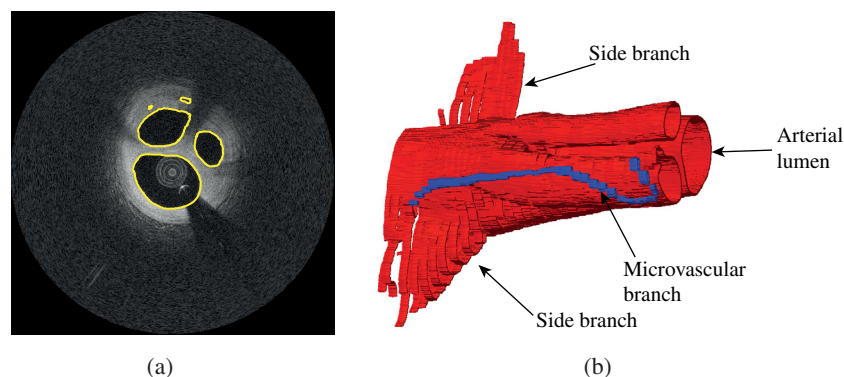

Fig. 10 Segmentation of multiple lumen using the proposed method. (a) Lumen shapes of various sizes have been simultaneously segmented using the proposed method. (b) 3-D visualization of the lumen geometry.

7 Comparison of the Proposed Segmentation Methods with Other Methods

The performance of the proposed segmentation method was compared with another contour evolution approach—the Chan–Vese[24] (CV) method and manual segmentation. The CV method has been employed for IV-OCT image segmentation,[1] whereas manual segmentation is still a gold standard for lumen segmentation and is commonly used for validating (as in Sec. 4) the techniques.

The CV method and local region-based ACM (Sec. 2.2) were applied to an IV-OCT image containing multiple lumen. The same initial ϕ derived from a particular binary mask was used in both cases. The final lumen contour generated by both approaches is shown in Fig. 11(a). The evolution of the local region-based contour stopped once it had arrived at the lumen boundary; however, the CV-based active contour progressed until the iteration stopped. Thus global region-based techniques such as CV method have limitations when the contrast is low.

Though a quantitative comparison of the manual and the proposed segmentation approaches has been provided in Sec. 4, a visual comparison of both techniques is done in Fig. 11(b). It can be observed that the automated method was able to generate a closely resembling lumen contour even though the contrast of the arterial cross-section was poor. Certain discrepancies can be noticed where the automated contour appears not to be as smooth as that of the manual contour. This may be due to the diffused boundaries of the low-contrast lumen.

8 Discussion

In this study, a lumen segmentation method was presented that can not only extract the lumen boundaries automatically from a 3-D image-stack, but can also handle blood artifacts and correct the contour for guide-wire artifacts and side-branches. Generally, a sequential approach is followed for lumen segmentation, where first the catheter, its covering sheath, and guide-wire are removed from the image and then the lumen is

segmented.[4] No such steps were required in the proposed method, as lumen intensity-enhanced IV-OCT images were used for segmenting the lumen boundaries. This was possible as a result of the large transmissivity (see Sec. 2.1) in the luminal region, which created a contrast between the lumen and its surrounding tissue and background regions.

Pullback datasets that provided various image processing challenges, shadowing effects, presence of residual blood, multiple lumen, low-contrast regions, and microvascular features were used in this current study. The ability of the proposed segmentation method to segment the lumen in the presence of these challenges proved the capability of the technique. Generally, the lumen segmentation method was implemented directly for a pullback stack using the ν, Δt, K, and N values determined for one of the frames in the stack. No human intervention was required when the true lumen boundary was the only one nearest to the zero level-set contour of ϕ. Sometimes when the contour was close to the abluminal borders of a plaque, it could evolve toward this boundary rather than the true lumen. This was due to the threshold level used in step 1.1, whereby nonluminal regions were also included in the ϕ_i. In such cases, the threshold level was modified and the lumen segmentation process (steps in Sec. 2.2) was repeated for those frames. In some images, blood-flow artifacts such as a blood column linking the lumen and the catheter or flowing very close to the wall could influence the contour evolution. In such cases, the parametric values were tuned so that true lumen was segmented quickly. As shown in Fig. 11(b), sometimes lumen regions associated with the lumen may have low contrast and depending upon the parametric values the contours may not be very smooth. In such cases, by tuning the parametric values the desired lumen smoothness can be achieved. However, during validation analysis no such corrections were performed during lumen segmentation. Thus, the ICC and Diff values for lumen segmentation in Table 2 can be further improved by using specific parametric values for the affected frames.

The contour compensation method discussed in Sec. 2.4 was applied only to mask out abnormal contour sections resulting from the degraded lumen boundaries at the far regions of the side-branch. The masked out sections can be interpolated as performed for the guide-wire. However, in Fig. 8(h) this was not preformed because at the first side-branch there was an overlapping guide-wire shadow, while the second side-branch extended beyond the imaging range.

In the present study, all the computing was performed serially in a MATLAB® environment. This increased the computational time as observed in Table 1. The processing times for polar-image conversion and anisotropy-based edge preserved image smoothing methods can be greatly reduced when performed in C or C++. The lumen segmentation method can be made 15 times faster by making the job parallel and implementing graphical processing units.[25]

While level-set-based localized region ACM was used in this study, alternate approaches such as MRF[7] or an EM[8] labeling method could also be applied to lumen intensity-enhanced IV-OCT images, to segment the lumen. The advantage of using lumen intensity-enhanced images are that the labeling technique can now cluster the lumen regions separately from the background regions, which was not possible in nonenhanced IV-OCT images. Thus, this transmissivity-based lumen intensity enhancement method allows direct segmentation of the lumen, instead of inferring it from the tissue boundaries.
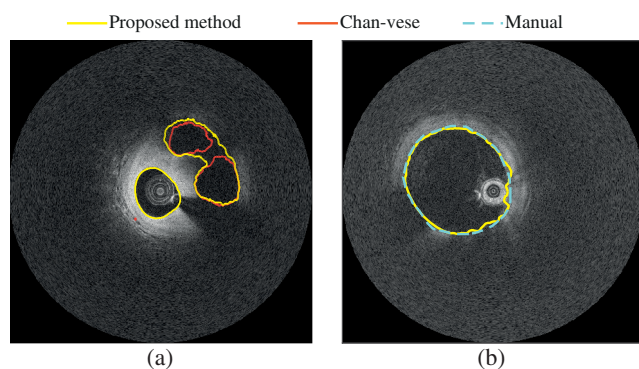

Fig. 11 Comparison of the proposed lumen segmentation with CV and manual segmentation methods. (a) Multiple lumens segmented by the current approach and CV technique (Video 2). Same initial ϕ was used in both cases. Contour for the CV method continued to evolve past the lumen boundaries until the iteration stopped while in the proposed the contour stopped to evolve at the true lumen. (b) Low-contrast lumen image segmented by both manual and localized level-set methods. Though both contours closely follow the same path, the manually obtained lumen is very smooth (Video 2, MPEG, 219 KB) [URL: http://dx.doi.org/10.1117/1.JMI.3.4.044001.2].

As improved IV-OCT systems are made clinically available and with high-density volume imaging,[26] it would be possible to construct microvascular beds associated with atherosclerosis in *in vivo* clinical cases. While this lumen segmentation method can identify blood-cleared microvessels, cross-correlation-based microvessel segmentation[22,23] can be used to extract other microvessels with blood flow in them. Both approaches when combined, can help in visualizing the complete microvasculature.

9 Conclusions

An automatic lumen segmentation approach for an IV-OCT pullback dataset was demonstrated, which combines the transmissivity property of luminal regions and the capability of the localized level-set segmentation method to extract luminal boundaries. The transmissivity-based mapping method enhanced the lumen intensity while the localized level-set method employed local speckle distribution properties to evolve the zero-level set function toward the object boundary. The technique performed adequately even in the presence of image artifacts such as loss of contrast and the presence of residual blood. The proposed segmentation tool also performs correction for guide-wire artifacts and accurately demonstrates side-branch openings.

Appendix: Derivation of Localized Gaussian Speckle Distribution-Based Level-Set ACM Method

The energy functional is derived on the assumption that the intensity-enhanced IV-OCT image has Gaussian-type speckle distribution, as shown in Eq. (5)

$$p(I) = \frac{1}{\sqrt{2\pi}\sigma} \exp\left[-\frac{(u-I)^2}{2\sigma^2}\right], \tag{5}$$

where σ and u denote the SD and mean of the pixel intensities at the selected region of the image.

As shown by Wang[18] et al., for any given local region $\mathcal{O}_x$ to be segmented on the basis of MAP requires that the product of the probability distribution in each subregion, namely $\mathcal{O}_x \cap \Omega_1$ and $\mathcal{O}_x \cap \Omega_2$, should be a maxima, [i.e., $\prod_{i=1}^{2}\prod_{y\in\mathcal{O}_x\cap\Omega_i} p_{i,x}[I(y)]$ is maximum, where $p_{i,x}[I(y)]$ follows Eq. (5)]. By taking a log of this term and introducing a minus sign, so that the energy is minimized, the image-dependent energy functional is defined. Thus, the energy minimization term for the localized region $\mathcal{O}_x$ is expressed as

$$E_x = \sum_{i=1}^{2} \int_{\mathcal{O}_x\cap\Omega_i} -\log p_{i,x}[I(y)]\mathrm{d}y. \tag{6}$$

Equation (6) can be generalized for any local region by defining a window function that can be introduced at any location of the image. Any region outside the window function will be masked out. $\mathcal{W}$ is the window function used in the current study and is expressed as

$$\mathcal{W}(x,y) = \begin{cases} 1, & \|x-y\| < r \\ 0, & \text{otherwise,} \end{cases} \tag{7}$$

where r is the radius parameter of the window.

Thus, Eq. (6) can be expressed as

$$E_x = \sum_{i=1}^{2} \int_{\Omega_i} -\mathcal{W}(x-y)\log p_{i,x}[I(y)]\mathrm{d}y. \tag{8}$$

As shown in Eq. (8), the $\mathcal{W}$ is centered at point x in the image. By integrating Eq. (8) over the entire image domain, $E = \int_\Omega E_x \mathrm{d}x$, the energy functional for the whole image can be obtained.

In this study, the closed contour C is considered to be the zero level-set of an implicit level-set function, ϕ, (i.e., contour, $C = \{\mathbf{x}:\phi(\mathbf{x}) = 0\}$). Thus for a given local region $\mathcal{O}_x$, the two regions Ω_1 and Ω_2 can be defined in terms of ϕ as $\Omega_1 = \{\mathbf{x}:\phi(\mathbf{x}) > 0\}$ and $\Omega_2 = \{\mathbf{x}:\phi(\mathbf{x}) < 0\}$. As both are disjoint regions, when the Heaviside function is applied to ϕ, each region can be identified. Thus rewriting Eq. (8) in terms of ϕ and the Heaviside function gives

$$E_x = -\int \mathcal{W}(x-y)\{\log p_{1,x}[I(y)]H_\varepsilon[\phi(y)]$$
$$+ \log p_{2,x}[I(y)]\{1 - H_\varepsilon[\phi(y)]\})\mathrm{d}y. \tag{9}$$

For computational implementation, in Eq. (9), a smoothed Heaviside function, H_ε is used and it is defined as

$$H_\varepsilon(x) = \frac{1}{2}\left[1 + \frac{2}{\pi}\arctan\left(\frac{x}{\varepsilon}\right)\right] \tag{10}$$

and its derivative δ_ε is defined as follows:

$$\delta_\varepsilon(x) = H'_\varepsilon(x) = \frac{1}{\pi}\frac{\varepsilon}{\varepsilon^2 + x^2}. \tag{11}$$

By integrating Eq. (9) for entire image domain, the energy E as a function of ϕ can be obtained. Generally, in level-set ACM methods a regularizing function, $\mathcal{L}$, that smooths the contour by penalizing its length is added to the energy functional. Thus the total energy functional is expressed as

$$\mathcal{F} = \int_\Omega E_x \mathrm{d}x + \nu\mathcal{L}(\phi)$$
$$= \int_\Omega -\int \mathcal{W}(x-y)(\log p_{1,x}[I(y)]H_\varepsilon[\phi(y)]$$
$$+ \log p_{2,x}[I(y)]\{1 - H_\varepsilon[\phi(y)]\})\mathrm{d}y\,\mathrm{d}x$$
$$+ \nu\int |\nabla H[\phi(x)]|\mathrm{d}x, \tag{12}$$

where $\nu > 0$ is the weighting constant.

For segmentation, this energy functional in Eq. (12) should be minimized. It can be noted that this energy functional is not only a function of ϕ but also of mean, u_i, and SD, σ_i, values for each i-th region, as a result of the probability function, $p_{i,x}$, in the equation. Therefore, to minimize the functional, in terms of its parameters u_1, u_2, σ_1, σ_2, a calculus of variation is used.[18] The expression for these parameters at which the energy is minimized can be obtained by applying the Euler–Lagrange equation [18] to Eq. (12) and is summarized here.

$$u_i(x) = \frac{\int \mathcal{W}(y-x)I(y)M_{i,\varepsilon}[\phi(y)]\mathrm{d}y}{\int \mathcal{W}(y-x)M_{i,\varepsilon}[\phi(y)]\mathrm{d}y}, \tag{13}$$

$$\sigma_i(x)^2 = \frac{\int \mathcal{W}(y-x)[u_i(x) - I(y)]^2 M_{i,\varepsilon}[\phi(y)]\mathrm{d}y}{\int \mathcal{W}(y-x) M_{i,\varepsilon}[\phi(y)]\mathrm{d}y}. \tag{14}$$

In Eqs. (13) and (14), $i = 1, 2$; $M_{1,\varepsilon}[\phi(y)] = H_\varepsilon[\phi(y)]$ and $M_{2,\varepsilon}[\phi(y)] = \{1 - H_\varepsilon[\phi(y)]\}$. Finally the energy functional in Eq. (12) is minimized in terms of ϕ, using a gradient descent method,[18] which gives the following gradient flow equation:

$$\frac{\partial \phi}{\partial t} = \delta(\phi) \int \mathcal{W}(y-x) \left\{ \log \left[\frac{\sigma_1(y)}{\sigma_2(y)} \right] + \frac{[u_1(y) - I(x)]^2}{2\sigma_1(y)^2} \right.$$
$$\left. - \frac{[u_2(y) - I(x)]^2}{2\sigma_2(y)^2} \right\} \mathrm{d}y + \nu\delta(\phi)\mathrm{div}\left(\frac{\nabla\phi}{|\nabla\phi|} \right). \tag{15}$$

Disclosures

No conflicts of interest, financial or otherwise, are declared by the authors.

References

1. Z. Wang et al., "Semiautomatic segmentation and quantification of calcified plaques in intracoronary optical coherence tomography images," *J. Biomed. Opt.* **15**, 061711 (2010).
2. G. J. Ughi et al., "Fully automatic three-dimensional visualization of intravascular optical coherence tomography images: methods and feasibility in vivo," *Biomed. Opt. Express* **3**, 3291–3303 (2012).
3. M. M. G. Macedo et al., "A bifurcation identifier for iv-OCT using orthogonal least squares and supervised machine learning," *Comput. Med. Imaging Graph.* **46**, 237–248 (2015).
4. A. Wang et al., "Fully automated side branch detection in intravascular optical coherence tomography pullback runs," *Biomed. Opt. Express* **5**, 3160–3173 (2014).
5. Z. Wang et al., "Volumetric quantification of fibrous caps using intravascular optical coherence tomography," *Biomed. Opt. Express* **3**, 1413–1426 (2012).
6. G. Unal, S. Gurmeric, and S. G. Carlier, "Stent implant follow-up in intravascular optical coherence tomography images," *Int. J. Cardiovasc. Imaging* **26**, 809–816 (2010).
7. S. Tsantis et al., "Automatic vessel lumen segmentation and stent strut detection in intravascular optical coherence tomography," *Med. Phys.* **39**, 503–513 (2012).
8. K. Tung et al., "Automatical vessel wall detection in intravascular coronary OCT," in *2011 IEEE Int. Symp. on Biomedical Imaging: From Nano to Macro*, pp. 610–613 (2011).
9. G. J. Ughi et al., "Automated tissue characterization of in vivo atherosclerotic plaques by intravascular optical coherence tomography images," *Biomed. Opt. Express* **4**, 1014–1030 (2013).
10. G. J. Tearney et al., "Consensus standards for acquisition, measurement, and reporting of intravascular optical coherence tomography studies: a report from the international working group for intravascular optical coherence tomography standardization and validation," *J. Am. Coll. Cardiol.* **59**, 1058–1072 (2012).
11. M. J. A. Girard et al., "Shadow removal and contrast enhancement in optical coherence tomography images of the human optic nerve head," *Invest. Ophthalmol. Visual Sci.* **52**, 7738–7748 (2011).
12. K. Vermeer et al., "Depth-resolved model-based reconstruction of attenuation coefficients in optical coherence tomography," *Biomed. Opt. Express* **5**, 322–337 (2014).
13. C. Xu et al., "Characterization of atherosclerosis plaques by measuring both backscattering and attenuation coefficients in optical coherence tomography," *J. Biomed. Opt.* **13**, 034003 (2008).
14. G. van Soest et al., "Atherosclerotic tissue characterization in vivo by optical coherence tomography attenuation imaging," *J. Biomed. Opt.* **15**, 011105 (2010).
15. M. Pircher et al., "Speckle reduction in optical coherence tomography by frequency compunding," *J. Biomed. Opt.* **8**, 565–569 (2003).
16. G. Vegas-Snchez-Ferrero, M. Martn-Fernndez, and J. M. Sanches, "A gamma mixture model for IVUS imaging," in *Multi-Modality Atherosclerosis Imaging and Diagnosis*, L. Saba et al., Eds., pp. 155–171, Springer, New York (2014).
17. S. Lankton and A. Tannenbaum, "Localizing region-based active contours," *IEEE Trans. Image Proc.* **17**, 2029–2039 (2008).
18. L. Wang et al., "Active contours driven by local gaussian distribution fitting energy," *Signal Process.* **89**, 2435–2447 (2009).
19. S. Aja-Fernndez and C. Alberola-Lpez, "On the estimation of the coefficient of variation for anisotropic diffusion speckle filtering," *IEEE Trans. Image Proc.* **15**, 2694–2701 (2006).
20. G. van Soest, J. G. Bosch, and A. F. W. van der Steen, "Azimuthal registration of image sequences affected by nonuniform rotation distortion," *IEEE Trans. Inf. Technol. Biomed.* **12**, 348–355 (2008).
21. N. S. van Ditzhuijzen et al., "Optical coherence tomography-guided bifurcation stenting of a coronary artery dissection," *Can. J. Cardiol.* **30**, 956.e11–956.e14 (2014).
22. S. Joseph et al., "Variation in cross-correlation as a discriminator for microvessel imaging using clinical intravascular optical coherence tomography systems," *Proc. SPIE* **8934**, 89342L1 (2014).
23. S. Joseph et al., "Developing cross-correlation as a method for microvessel imaging using clinical intravascular optical coherence tomography systems," *Biomed. Opt. Express* **6**, 668–689 (2015).
24. T. Chan and L. Vese, "Active contours without edges," *IEEE Trans. Image Proc.* **10**, 266–277 (2001).
25. E. Smistad et al., "Medical image segmentation on gpus a comprehensive review," *Med. Image Anal.* **20**, 1–18 (2015).
26. T. Wang et al., "Heartbeat OCT: in vivo intravascular megahertz-optical coherence tomography," *Biomed. Opt. Express* **6**, 5021–5032 (2015).

Shiju Joseph received his PhD in mechanical, aeronautical and biomedical engineering from the University of Limerick, Ireland, in 2012. Currently, he is a postdoctoral research scientist at Department of Cardiovascular Sciences, University of Leicester, UK, where he is involved in developing image processing and analysis methods for clinical imaging modalities such as optical coherence tomography (OCT) and computed tomography (CT) techniques.

Asif Adnan is an intervention cardiology trainee, currently working towards completing his clinical training as a cardiologist at Trent Cardiac Centre, Nottingham, UK. He is also an honorary clinical research fellow at the Department of Cardiovascular Science of University of Leicester, UK. He has been undertaking research on postmortem application of coronary OCT for last 3 years and currently writing up his doctoral thesis.

David Adlam is an associate professor in acute and interventional cardiology at Department of Cardiovascular Sciences, University of Leicester, UK, and practices interventional cardiology at Glenfield General Hospital. He leads a research team which is focused on developing clinically applicable imaging techniques that will allow better understanding of coronary artery disease (CAD).